Tenth International Conference on Computational Fluid Dynamics (ICCFD10), Barcelona,Spain, July 9-13, 2018

ICCFD10-146

Computational Aeroacoustics beneath High Speed Transitional and Turbulent Boundary Layers

K. Ritos, D. Drikakis and I. W. Kokkinakis
Corresponding author: konstantinos.ritos@strath.ac.uk

Department of Mechanical & Aerospace Engineering, University of Strathclyde, Glasgow, UK.

Abstract: This paper concerns a study of pressure fluctuations beneath hypersonic shock-wave turbulent boundary layer interactions and the associated acoustic loading on a compression/expansion ramp. We have employed high-order implicit large eddy simulations and conducted simulations at Mach 7.2. The spectral analysis of the pressure fluctuations at various locations of the compression/expansion ramp are compared with the spectra calculated beneath a hypersonic transitional boundary layer. Similarities and differences between the two hypersonic boundary layers, in the context of acoustic loading, are drawn. Extremely high values of pressure fluctuations are recorded after the shock re-attachement where the maximum pressure gradients are also observed, indicating that acoustic loading is correlated with areas of high pressure gradients. Finally, we show the impact of the boundary layer state (attached flow, turbulence bursts, recirculations, shock oscillations, shock re-attachment and expansion fans) on the frequency spectrum of the pressure fluctuations.

Keywords: Aeroacoustics, Hypersonic flows, Transition, Compressible flow, iLES.

1 Introduction

Pressure fluctuations beneath supersonic and hypersonic transitional or turbulent boundary layers (TBL), and to a greater extent shock-wave turbulent boundary layer interaction (STBLI), are a dominant source of acoustic fatigue that structural elements of aircrafts are exposed to. Subsonic and supersonic TBL have been studied extensively leading to a significant amount of theoretical publications concerning the amplitude of pressure fluctuations [1] as well as the roll-off of the pressure spectrum [2, 3, 4]. These models and theories have been validated experimentally [5, 6, 7, 8] and also verified numerically [9, 10].

To date, there has been no systematic attempt to investigate the effect of hypersonic transitional boundary layers or STBLI on acoustic loading. Past numerical [11, 12] and experimental [13, 14, 15, 16] studies of hypersonic STBLI have focused on the structure of turbulence. For instance, Görtler-like vortices have been observed at Mach 7 around a compression ramp and it was suggested that these vortices are responsible for the low-frequency motion of the shock wave [12]. Studies of hypersonic TBLs have also been published [17, 18]; however investigations of the effects of transitional or turbulent boundary layers on acoustic loading are scarce [19, 20].

In this paper, we present a spectral analysis of pressure fluctuations beneath hypersonic STBLI by performing implicit Large Eddy Simulations (iLES) of a Mach 7.2 turbulent boundary layer over a 33° compression ramp. The ramp angle and free-stream properties have been chosen according to the experimental set up of Schreyer et al. [16]. It is expected that one or more shocks will form in the supersonic and hypersonic parts of the flow. The flowfield is affected by the interaction between this shock system and the incoming turbulent boundary layer. In this interaction region large gradients of pressure will occur.

Furthermore, we will show the pressure fluctuations and their frequency spectrum at two locations of a hypersonic transitional boundary layer, with one being at the end of the transition to turbulence region and the other in the fully turbulent region. This will allow to showcase similarities and differences between

the various hypersonic boundary layers in the context of acoustic loading. The flow results for the STBLI case have been previously compared with available Direct Numerical Simulations (DNS) and experimental data [21], while the results for the transitional boundary layer presented here are based on a previous more detailed study by the authors [20].

2 Governing equations and numerical modeling

We have employed the iLES approach in the framework of the in-house block-structured mesh code CNS3D [22, 23, 24] that solves the full Navier-Stokes equations using a finite volume Godunov-type method for the convective terms, whose inter-cell numerical fluxes are calculated by solving the Riemann problem using the reconstructed values of the primitive variables at the cell interfaces. A one-dimensional swept unidirectional stencil is used for reconstruction. The Riemann problem is solved using the so-called "Harten, Lax, van Leer, and (the missing) Contact" (HLLC) approximate Riemann solver [25, 26]. The 9th-order Weighted-Essentially-Non-Oscillatory (WENO) scheme [27] has been implemented in conjunction with the HLLC solver. The viscous terms are discretized using a second-order central scheme. The solution is advanced in time using a five-stage (fourth-order accurate) optimal strong-stability-preserving Runge-Kutta method [28].

2.1 Hypersonic flow over a flat plate

Two flow cases are considered here, with the first one being a hypersonic flow over a flat plate subjected to von Kármán atmospheric spectrum at the inlet. The flow transitions to fully turbulent at a downstream location, as shown in Figure 1 by isosurfaces of compressible Q-criterion[29, 30] and contour plots of density and temperature. The results presented here are from simulations performed at Mach 6 and turbulence intensity of the free-stream velocity $Tu = 3\%$. Further details about the free-stream and boundary conditions can be found in [20].

A mesh independence study was performed using three meshes, $G1 = 661 \times 161 \times 91$, $G2 = 811 \times 201 \times 121$ and $G3 = 1001 \times 251 \times 151$. All meshes are relatively fine and qualitatively comparable to previous DNS simulations of fully-turbulent hypersonic flows [31, 19]. The transition point and the shape factor H (Figure 2) are similarly predicted by the different mesh sizes. The shape factor H is used to assess the compressible boundary layer flow; H is defined as the ratio of the displacement thickness (δ^*) to the momentum thickness (θ):

$$H = \frac{\delta^*}{\theta} = \left[\int_0^\infty \left(1 - \frac{\rho(y)u(y)}{\rho_\infty u_\infty}\right) dy\right] \left[\int_0^\infty \frac{\rho(y)u(y)}{\rho_\infty u_\infty} \left(1 - \frac{u(y)}{u_\infty}\right) dy\right]^{-1}, \tag{1}$$

where u_∞ and ρ_∞ are the freestream velocity and density, respectively. Previous studies [32, 33, 34, 35] have confirmed the reduction of the shape factor with increasing Reynolds number and the potential asymptotic limit at high Reynolds numbers. A correlation formula for fully turbulent boundary layers and for a broad range of Reynolds numbers has been proposed in the literature [35]

$$H_{comp} = H_{inc} + 0.4M^2 + 1.222\frac{T_w - T_{aw}}{T_\infty}, \tag{2}$$

where $H_{inc} = 1.4$. The present simulation results are compared with the above formula in Figure 2 showing good agreement. Averaged flow statistics are computed by averaging in time over three flow cycles and spatially in the spanwise direction. The total simulation time is equal to six flow cycles.

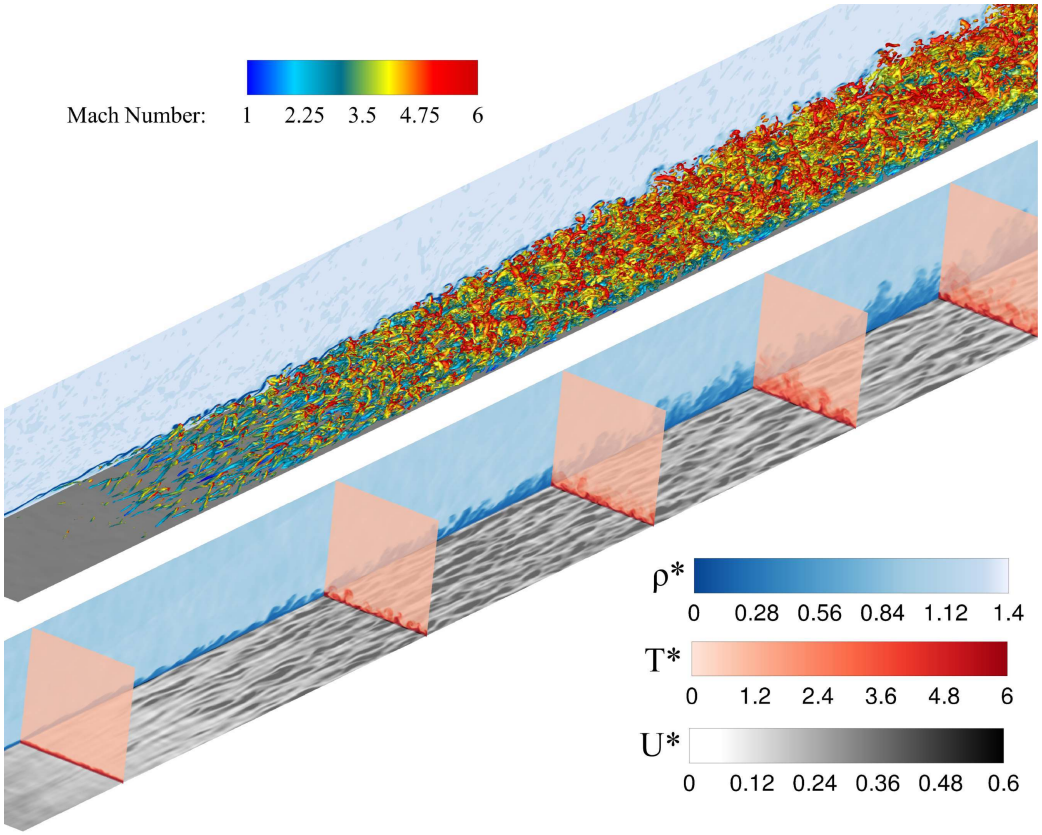

Figure 1: Isosurfaces of compressible Q-criterion coloured by Mach number. The density gradient is also plotted in grayscale on the side of the graph highlighting the transition region. Contour plots of density and streamwise velocity near the wall, as well as temperature contour plots at various cross sections of the simulation domain, are also shown.

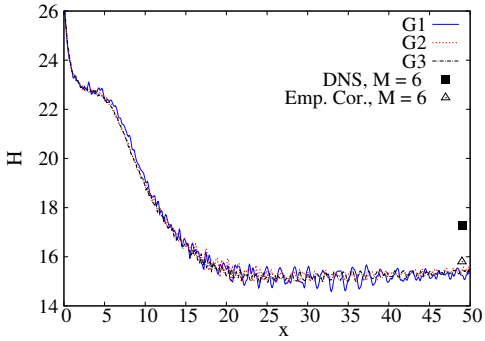

Figure 2: Shape factor H development along the plate for three mesh resolutions. An empirical correlation (Eq. 2) and DNS data[36] are also presented for the fully turbulent flow regime.

2.2 Hypersonic flow over a compression/expansion ramp

The second case considered here is a hypersonic flow over a $\alpha = 33°$ compression ramp followed by an expansion corner with the same deflection angle (Figure 3). The incoming flow corresponds to a turbulent boundary layer at Mach 7.2 with a thickness $\delta = 5$ mm. Based on the free-stream properties (Table 1) and the reference length δ, the incoming flow has a Reynolds number of $Re_\delta = 102{,}731$. Periodic boundary conditions are implemented in the span-wise direction (z) . In the wall-normal direction (y), a no-slip isothermal wall

(with a temperature T_w of 340 K) is used [37]. High-order implementation of the boundary conditions requires fictitious cells to be added inside the wall. The velocity components on these cells are linearly extrapolated from the computational cells inside the domain. The temperature is also linearly extrapolated using the specified wall temperature. The density is calculated from the equation of state considering zero pressure gradient normal to the wall. Supersonic outflow conditions are applied to the outlet and far-field conditions are applied to the upper boundary. A synthetic turbulent inflow boundary condition is used to produce a freestream flow with a superimposed random turbulence.

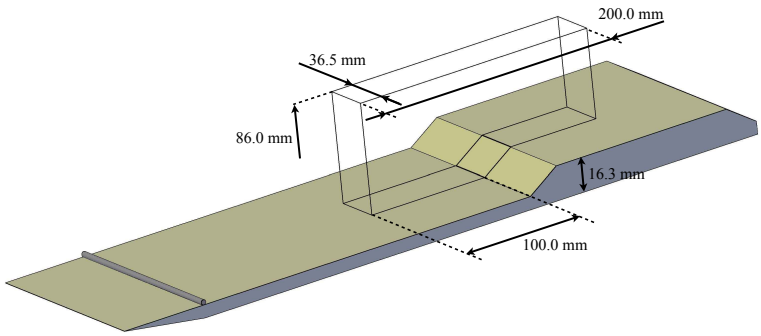

Figure 3: Schematic representation of the simulation domain with dimensions in mm.

Table 1: Simulation parameters

δ (mm)	U_∞ (m/s)	P_∞ (Pa)	T_∞ (K)	M_∞
5.0	1,146	1,365.6	63.06	7.2
ρ_∞ (kg/m^3)	T_w (K)	Re_δ	Re_θ	Re_τ
0.0755	340	102,731	3,500	198

The synthetic turbulent inflow boundary condition is based upon the digital filter (DF) method documented in [38, 39, 40] and, specifically validated in the framework of the present iLES code CNS3D in [41, 42, 23]. According to DF, instead of using a white-noise random perturbation at the inlet, energy modes within the Kolmogorov inertial range scaling with $k^{-5/3}$, where k is the wavenumber, are introduced into the turbulent boundary layer. Opposite to the von Kármán atmospheric spectrum introduced at the inlet of the first case, the DF does not introduce any large-scale energy modes scaling with k^4. A cutoff at the maximum frequency of 50 MHz is applied, since the finest mesh used in this study would under-resolve higher values. The turbulence intensity at the inlet (Tu) is set as 3% of the intensity of the freestream velocity.

Following typical resolution recommendations for LES and DNS simulations [43, 44, 10] three relative fine meshes were used in this study ranging from fine wall-resolved LES (G1) to under-resolved DNS (G3). The mesh is clustered near the corner in the stream-wise direction and near the wall in the wall-normal direction. The number of mesh points and the mesh spacing are summarized in Table 2 along with the LES and DNS recommendations from the literature. The present mesh spacing (Δy) is scaled using the conventional inner variable method $\Delta y^+ = u_\tau \Delta y/\nu_w$, where $u_\tau = \sqrt{\tau_w/\rho_w}$ is the friction velocity, ν_w is the near wall kinematic viscosity, τ_w is the near wall shear stress, and ρ_w is the near wall density. A mesh convergence study was performed in [21] with the two finer meshes, G2 and G3, showing close agreement in all calculated quantities and justifying the use of G3 in the further analysis.

The structure of turbulence at the compression/expansion ramp is clearly visualized by iso-surfaces of the compressible Q-criterion[29, 30] for all meshes in Figure 4. The iso-surfaces are colored with the stream-wise velocity showing the flow separation at the corner. The density gradient is also plotted in greyscale indicating the position and the thickness of the shock. The flow statistics are computed by averaging in time

Table 2: Mesh parameters

	N_x	N_y	N_z	Δx^+_{min}	Δx^+_{max}	Δy^+_w	Δy^+_e	Δz^+
G1	401	167	107	11.48	41.14	1.0	7.37	13.48
G2	601	249	161	7.7	27.35	1.0	4.26	8.96
G3	801	333	213	5.77	20.4	0.5	3.65	6.77
LES[43, 44, 10]	–	–	–	50	150	≤ 1.0	–	15–40
DNS[43, 44, 10]	–	–	–	10	20	< 1.0	–	5–10

over at least seven flow-throughs and spatially in the span-wise direction. The total simulation time for each case is equal to at least twelve flow-throughs, with the first five omitted from the calculations for statistical purposes. The statistical convergence of the simulations has been tested by comparing the results between fifteen and seven flow-throughs using mesh G1 resulting in less than 2% difference.

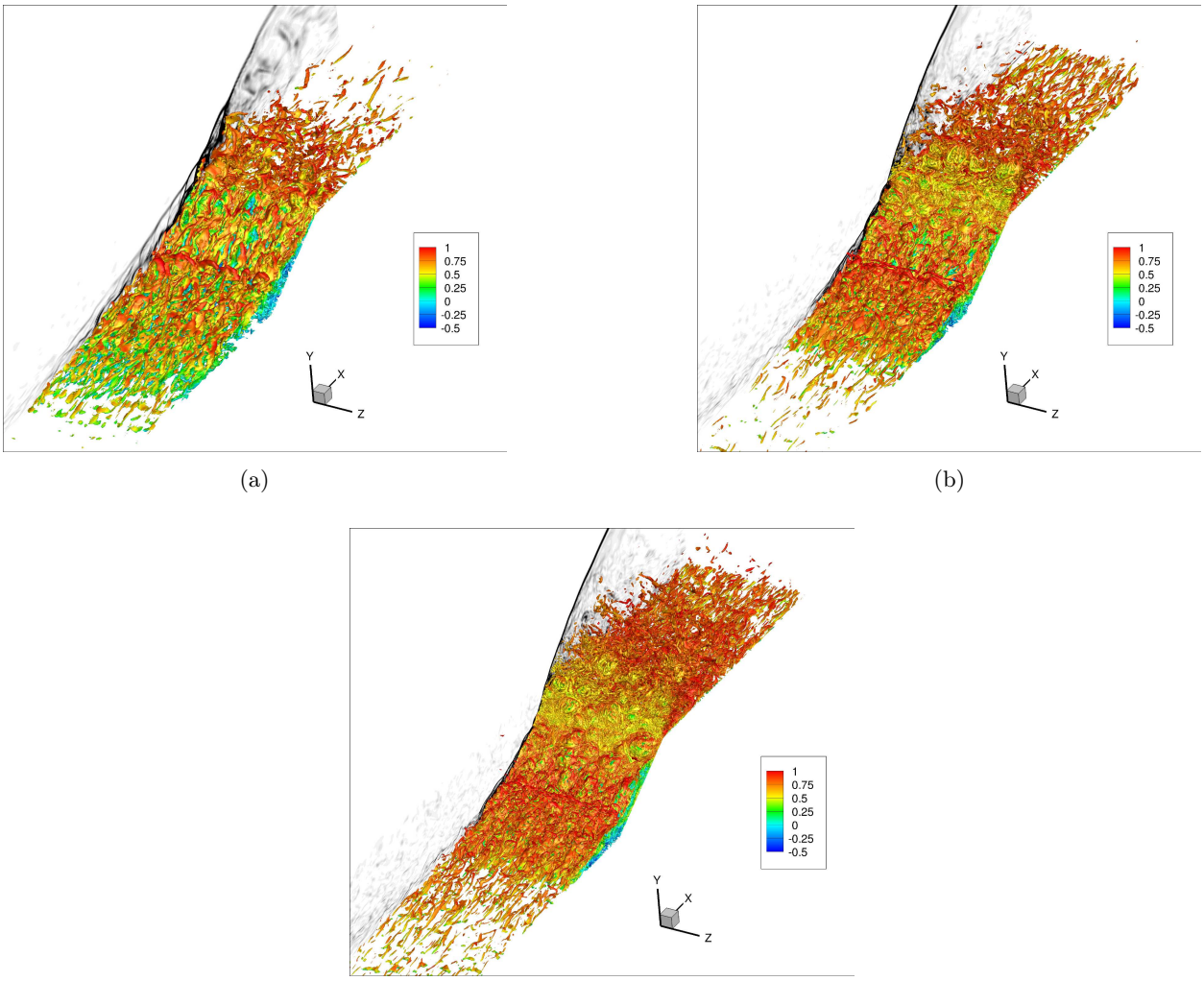

(a) (b)

(c)

Figure 4: Isosurfaces of compressible Q-criterion coloured by streamwise velocity indicating the flow separation at the corner. The density gradient is also plotted in grayscale at the side of the plot highlighting the position and the thickness of the shock.

For a better visualisation of the flow separation we show the flowfield streamlines over a temperature

contour plot in Figure 5. In the re-circulation area the temperature is significantly higher compared to the free-stream conditions, reaching a maximum of 570 K at the re-attachment point. In the following section we will show how the various changes in the flow field (separation, re-circulation, re-attachment, expansion, etc.) affect not only the magnitude of the acoustic loading but also its spectral characteristics.

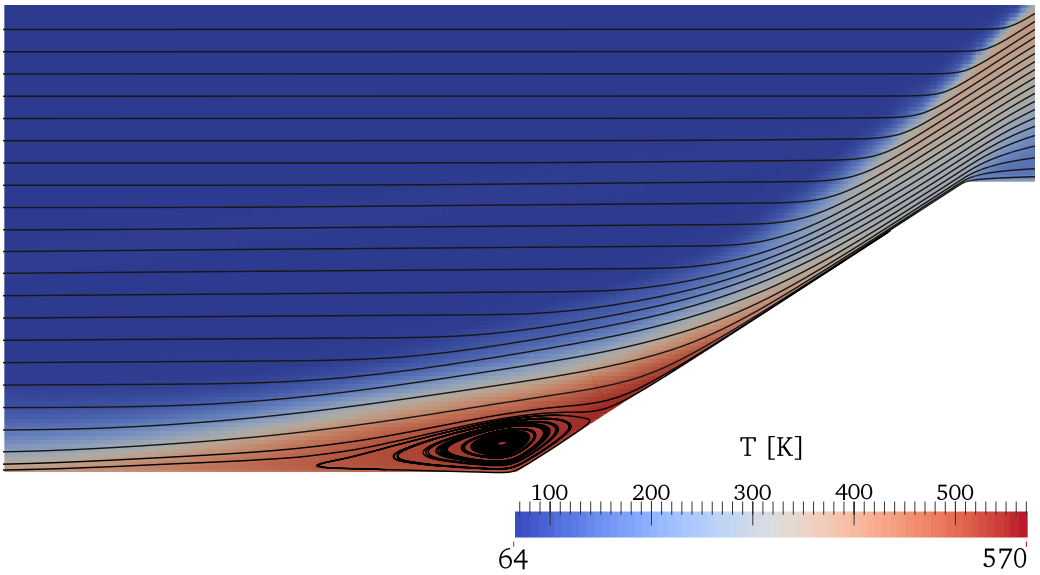

Figure 5: Flowfield streamlines and temperature contour plot in the region of the compression/expansion ramp. All variables have been averaged over time and in the spanwise direction.

The density gradients in Figure 4 indicated the position and thickness of the lambda shock. In Figure 6 we plot the magnitude of the pressure gradient ($|\nabla P|$) averaged in the spanwise direction and in time. The formation of a lambda shock is clearly evident in this figure, while two other areas with high pressure gradients can also be identified. The first one is the expected expansion fan created at the expansion corner of the ramp. The second is an area above the re-attachment of the flow on the ramp and very close to the wall. This area is highlighted in inset (b) of Figure 6 where red colour indicates the maximum values of pressure gradient calculated near the wall.

Laganelli et al. [1] proposed a theoretical model for P'_{rms}/q_∞ beneath compressible fully turbulent attached boundary layers, where $q_\infty = (\rho_\infty u_\infty^2)/2$ is the dynamic pressure and u_∞ is the free-stream velocity. The model is based on fitting incompressible measurements [45, 46, 47, 48] to compressible flows by taking into account the wall temperature and free-stream Mach number:

$$\frac{P'_{rms}}{q_\infty} = \frac{0.006}{\left[0.5 + (T_w/T_{aw})\,(0.5 + 0.09M_\infty^2) + 0.04M_\infty^2\right]^{0.64}}, \tag{3}$$

where T_{aw} is the adiabatic wall temperature calculated from the recovery temperature. Previous studies [8, 49, 50, 51] have suggested that the value in the numerator of Eq. 3 should be between 0.008 and 0.010, with [6] suggesting an Re_θ dependence. Beresh et al. [8] has proposed a value of 0.009 for the incompressible limit based on an estimated extension of the measured pressure spectra. According to the simulations in [20], a value of 0.008 is suggested for flows up to Mach 8. The theoretical model with the suggested value (dashed black line in inset (a) of Figure 6) shows good agreement with the calculated values in the areas of the domain where the flow is attached and the pressure gradients are low. In the recirculation region the (normalised) pressure fluctuations increase, while extremely high values are recorded after the re-attachment of the flow where the maximum pressure gradients are also observed (Insets (a) and (b) of figure 6). This is a strong indication that acoustic loading is correlated with areas of high pressure gradients.

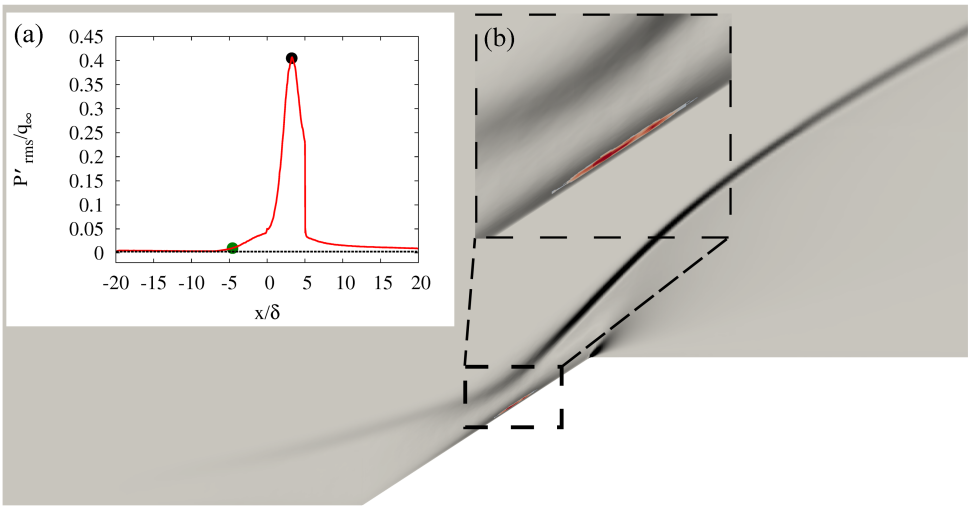

Figure 6: Magnitude of pressure gradient ($|\nabla P|$) over the simulation domain. Darker (black) areas indicate higher $|\nabla P|$. Inset (a) is the root mean square of wall pressure fluctuations (P'_{rms}) along the wall normalised by the freestream dynamic pressure, q_∞. The black dashed line represent theoretical predictions based on Eq.3 with $T_w/T_{aw} = 0.524$; see discussion in the text. The green filled circle is the foot of the recirculation bubble. The black filled circle is the point of maximum $|\nabla P|$. Inset (b) magnifies the area of the highest $|\nabla P|$ on the wall. Red colour in that case indicates high $|\nabla P|$.

3 Acoustic loads

Our main interest in this study is to perform acoustic loading calculations at various locations of a compression/expansion corner under hypersonic conditions and compare these results with calculations performed beneath hypersonic transitional and turbulent boundary layers. From the analysis in the previous section, acoustic loads are expected to peak at the re-attachment point, obtaining significantly higher values than those sustained in the rest of the domain. A representative quantity of acoustic loading is the overall Sound Pressure Level (SPL) that is directly linked to high cycle fatigue of aerospace structures. This quantity can be obtained through the transformation of pressure fluctuations, SPL $= 20\log_{10}(P'/P_0)$ dB, where $P_0 = 20\mu$Pa.

In Figure 7 we show the SPL over the whole simulation domain, highlighting the re-attachment region where values in excess of 170 dB are observed, significantly higher than the 140 dB observed in the TBL region before the separation bubble and the 145 dB after the expansion corner. The re-attachment point, as well as the exact magnitude of the acoustic load, are important for the structural design of hypersonic vehicles. In the same figure we also show five positions that we selected for further analysis. These points are representative of the different flowfield conditions encountered in this simulation. More specifically the first position is away from the compression ramp and before the recirculation bubble where the flow can be considered attached and fully turbulent. The second location is close to the foot of the lambda shock where oscillations of the shock will be revealed through the pressure history calculation. The third position is in the recirculation bubble where the flow is detached, while the fourth position is close to the re-attachment point where maximum SPL values where calculated. Finally, the last position is just after the expansion fan where the flow is attached and fully turbulent but under different conditions compared to the first position.

In Figures 8(a) to 8(e) we show the normalised pressure histories at the selected locations, while in Figures 8(f) and 8(g) we compare the pressure histories from the first three and the last three positions, respectively. All time history plots have been recorded from the 5^{th} until the 12^{th} flow cycle (t_c). The lowest pressures are recorded at the first position (Figure 8(a)) while the highest at the fourth position (Figure 8(d)) where the flow is re-attached. The calculated pressures close to the re-attachment point are at least an order of magnitude higher than those calculated at other locations (for a comparison see Figures 8(f) and 8(g)). Interestingly enough, the pressure history of the second position (Figure 8(b)) exhibits values much higher than the average ones at periodic intervals. These high pressure values can be attributed to the

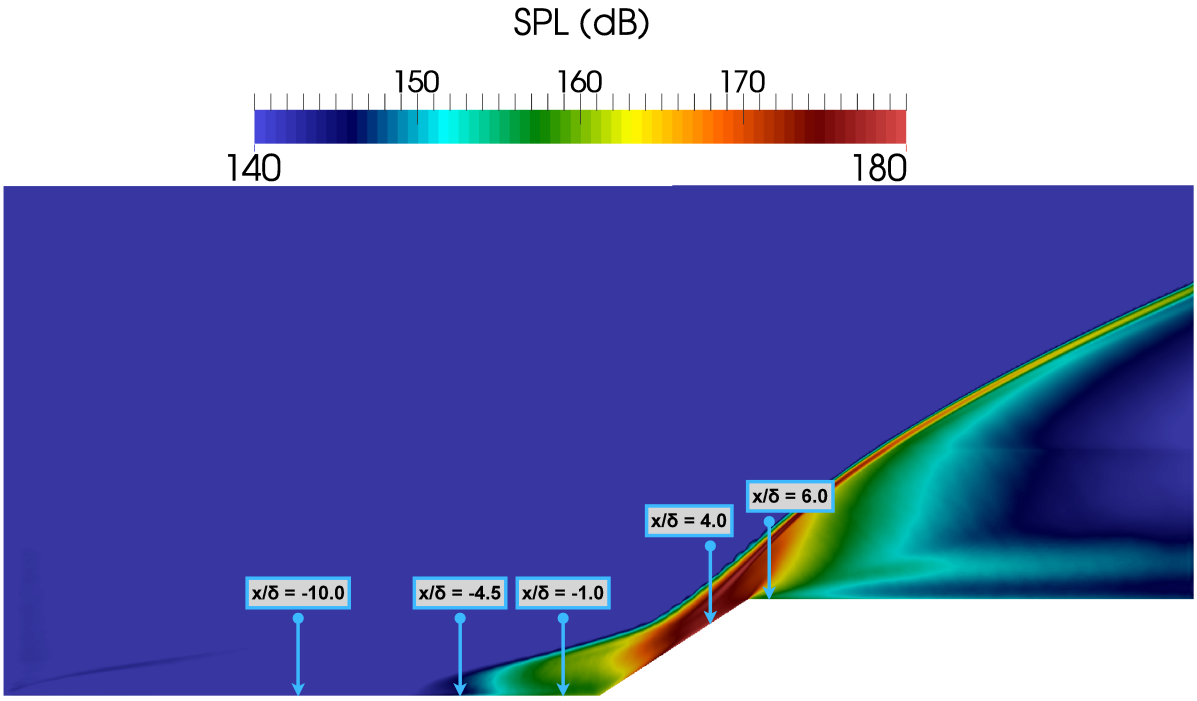

Figure 7: Sound pressure levels contour plot and locations of spectral analysis.

oscillation of the lambda shock over this location.

While the calculation of pressure and pressure fluctuations are indicative of the acoustic loading imposed on the wall, it is equally important to study the frequency content of these fluctuations. We use the Welch method [52] to calculate the power spectral density (PSD) of the pressure fluctuations at specific locations. For the compression/expansion corner flow the sampling frequency is approximately 16 MHz, and the overall pressure record is subdivided into 8 segments, each including $2 \times 1,200$ samples; note that we observe a negligible difference between the PSD produced using 8 and 12 segments. Details regarding the PSD calculation approach on the flat plate can be found in [20], where it was previously used for hypersonic transitional and turbulent boundary layer over a flat plate. The present spectral analysis of the pressure fluctuations on the wall is based on the single-point spectrum in the frequency domain which is defined as

$$\Phi(\omega) = \frac{1}{2\pi} \int_{-\infty}^{\infty} \overline{P'(x,y,z,t)P'(x,y,z,t+\tau)} e^{-i\omega\tau} d\tau, \tag{4}$$

where τ is a time delay and ω is the radial frequency.

The spectral behaviour of attached fully turbulent boundary layers in both subsonic and supersonic flows has been studied extensively. Bull [49] isolated four different regions of low, mid (which includes the spectral peak), mid-to-high overlap, and high frequencies, with corresponding spectrum slopes of ω^2, ω^0, ω^{-r} ($r = [0.7, 1.1]$), and ω^{-t} ($t = [7/3, 5]$), respectively. The low frequency region is influenced by the turbulent motion in the outer part of the boundary layer, while high frequencies are influenced by the viscosity and turbulent motion in the inner part of the boundary layer.

The spectrum roll-off at the same locations of the compression/expansion ramp where the pressure histories were recorded are shown in Figure 9. In addition, we show the spectrum roll-off at two locations of the boundary layer over the flat plate, one at the end of the transition region and one in the fully turbulent region (Figure 10).

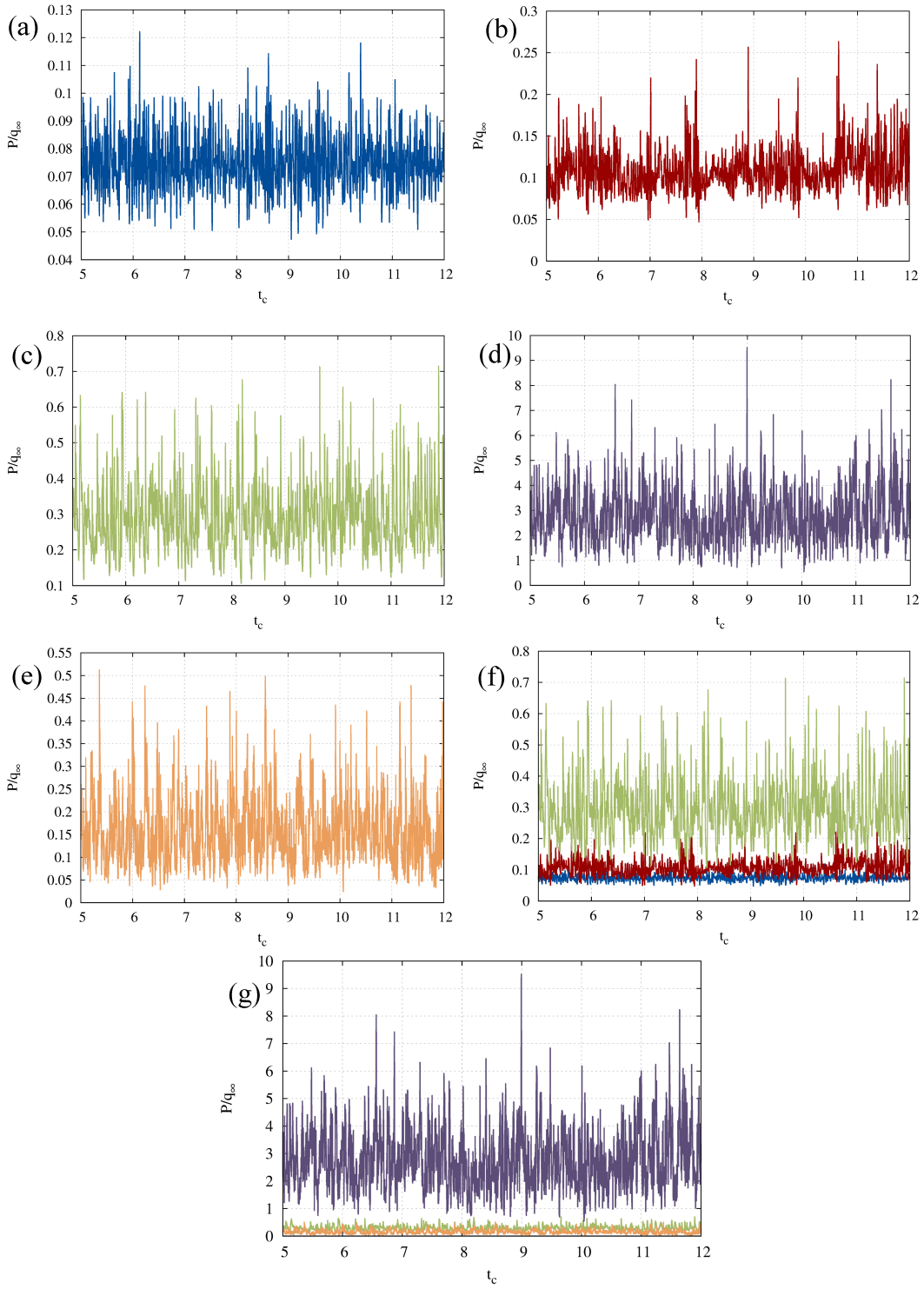

Figure 8: Pressure history at various locations on the ramp wall. Pressure is normalised by the dynamic freestream pressure (q_∞) and t_c is the time normalised by the time needed for one flow cycle. The pressure histories correspond to the following locations: (a) $x/\delta = -10$, (b) $x/\delta = -4.5$, (c) $x/\delta = -1$, (d) $x/\delta = 4$, and (e) $x/\delta = 6$. (f) shows a comparison of the pressure histories in the first three locations, while (g) for the last three locations.

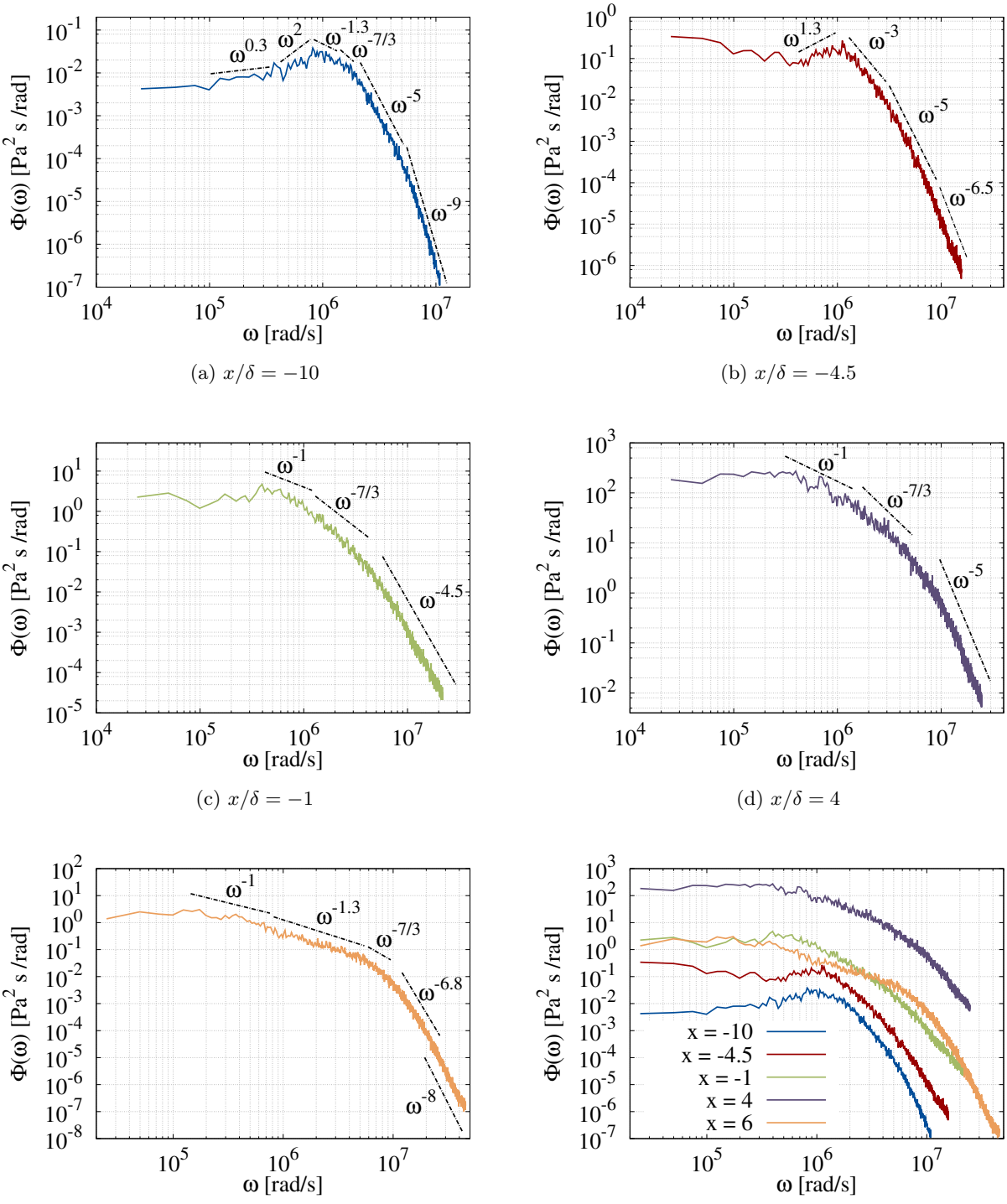

(a) $x/\delta = -10$

(b) $x/\delta = -4.5$

(c) $x/\delta = -1$

(d) $x/\delta = 4$

(e) $x/\delta = 6$

(f) All positions

Figure 9: PSD at various locations on the compression/expansion corner. Figure (f) is comparison of the spectra among all the locations under consideration.

According to the theoretical arguments made by Ffowcs-Williams [2] for compressible flows, in the low frequency region the scaling should follow $\omega \to 0$. This observation has been confirmed by experimental and numerical studies of supersonic and hypersonic turbulent boundary layers [19, 53, 8, 9]. This is in contrast to the Kraichnan-Phillips theorem for incompressible flows [49, 54, 55], which suggests ω^2. In our calculations

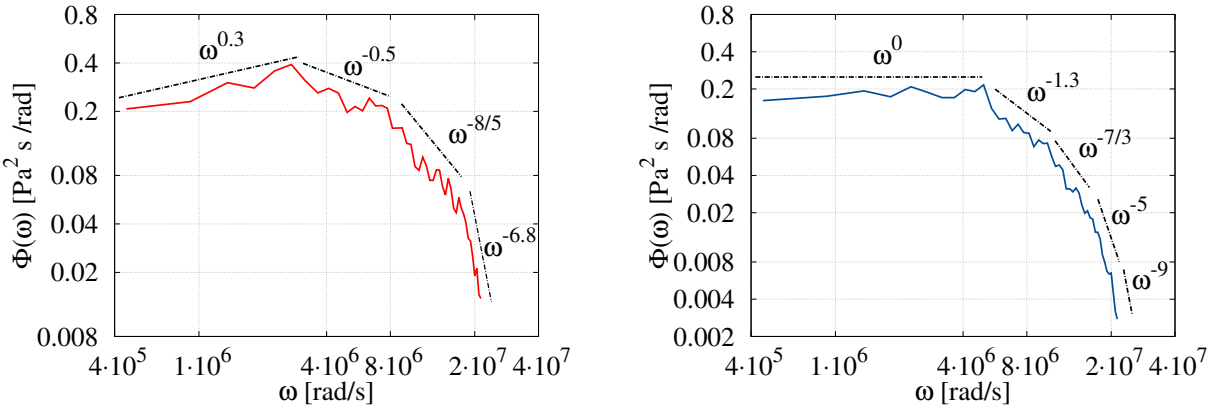

(a) End of the transition region

(b) Fully turbulent region

Figure 10: PSD at two locations beneath the hypersonic boundary layer over a flat plate.

the low frequency region yields $\omega \to 0$, which agrees with the aforementioned analysis. The only exception to this scaling is shown in the spectrum roll-off at the end of the transition region on the flat plate (Figure 10a) where the simulations yield $\omega^{0.3}$.

The mid-to-high overlap frequency region appears at sufficiently high Re_θ values and the spectrum varies as ω^{-r} with $r = 0.7$ to 1.1, influenced by the local Reynolds number. This region is associated with pressure-induced eddies in the logarithmic region of the boundary layer. Its scaling behaviour was predicted by Bradshaw [3], and was verified theoretically [56] and experimentally [8, 6]. This frequency region can be identified in all but one calculation points on the ramp and also on the fully turbulent region of the flat plate. The value of r lies between 1.0 to 1.3 depending on the location. The calculations at the foot of the lambda shock (Figure 9c) did not produce this scaling region while the scaling at the end of the transition region is $\omega^{-0.5}$. It should be noted that in our calculations the first two positions produced a sudden spectrum rise with a scaling up to ω^2 in a short frequency range. We believe that this frequency increase is related to the incoming turbulence produced by the digital filter and the motion of the lambda shock in the case of the second position but further investigation is required.

Following the mid-to-high overlap frequency region, the spectrum becomes $\omega^{-7/3}$, henceforth called "acoustic-transition", predicted for isotropic turbulence by Batchelor [57] and observed in various experiments [58, 59, 60], as well as verified by numerical calculations of supersonic turbulent boundary layers [19, 9]. This "acoustic-transition" region is present in all the calculated spectra and it is more clear to identify in the spectra calculated inside the re-circulation bubble (Figure 9c) and close to the re-attachment point (Figure 9d).

The scaling of this frequency region is slightly steeper (ω^{-3}) in the spectrum calculated beneath the foot of the lambda shock while it is shallower ($\omega^{-8/5}$) in the spectrum calculated at the end of the transition region. We believe that the oscillating shock and turbulence bursts, for the compression/expansion ramp and the flat plate, respectively, are responsible for the slope change in this frequency region. The theoretical prediction for this frequency region by Batchcelor was based on the assumption of isotropic turbulence. The deviation of the scaling behaviour from $\omega^{-7/3}$ may be due to the onset of flow anisotropy and localised coherent structures; however, this requires further investigation.

At high frequencies the spectrum decays more rapidly reaching a slope proportional to ω^{-5}. Sources in the sublayer ($y^+ < 20$) contribute to this frequency region according to the theoretical prediction of Blake [4], with the scaling being validated experimentally, as well [6, 5]. This frequency region appears in all calculations. In two cases the slope is steeper scaling as $\omega^{-6.8}$; These are the last location close to the expansion fan in the case of the ramp and the transition region in the case of the flat plate, respectively.

Additionally, in some locations on the ramp (see Figures 9a, 9b and 9e) and also in the fully turbulent region of the flat plate the last leg of the high frequency encompasses a region of (approximately) ω^{-8}. We attribute this region to high-speed, compressibility effects closer to the wall ($y^+ < 20$). A Mach number dependence of the spectrum in fully turbulent boundary layers that lead to steeper gradients has also been observed in experiments [61] and numerical simulations [19].

4 Conclusions

Acoustic effects beneath hypersonic transitional and turbulent boundary layers have been investigated by performing spatial and spectral analysis of near-wall pressure fluctuations. Simulations of two different flows, over a flat plate at Mach 6 and over a compression/expansion corner at Mach 7.2, have been carried out. The simulations have also been validated against theoretical, DNS and experimental data, where available. The most important conclusions drawn from the present study are summarised below:

- The modified Laganelli's theoretical model is valid for fully turbulent attached boundary layers but under-predicts the pressure fluctuations beneath re-circulations or areas of high pressure gradients.
- High SPL values are associated with shock re-attachment and structural panels will be subjected to the strongest acoustic fatigue in this region.
- Spectral analysis was performed at various points on the compression/expansion ramp and compared with calculations at points of the flow over a flat plate. This analysis highlighted similarities between the transition region on the flat plate and the point beneath the lambda shock on the expansion/compression ramp, where turbulence bursts and shock motion, respectively, alter the spectrum shape from the one expected beneath turbulent boundary layers.
- The frequency spectrum depends on the boundary layer conditions (attached flow, recirculations, shock oscillations, shock re-attachment and expansion fans).
- The pressure fluctuations calculated on the compression/expansion ramp are governed by scaling laws that are generally in agreement with those found in attached fully turbulent flows.
- In areas where the boundary layer is attached, a region of very high frequencies with a slope proportional to ω^{-8} was observed. This region is related to high-speed, compressibility effects near the wall.

Acknowledgments

This work was sponsored by the Air Force Office of Scientific Research, Air Force Material Command, USAF, under grant number FA9550-14-1-0224. The U.S. Government is authorised to reproduce and distribute reprints for Governmental purpose notwithstanding any copyright notation thereon. The authors would like to thank S. M. Spottswood, Z. Riley and D. Garner for their support. The authors would also like to thank EPSRC for providing access to computational resources on the National HPC facility ARCHER (http://www.archer.ac.uk) through the UK Applied Aerodynamics Consortium Leadership Project "e529".

References

[1] A. L. Laganelli, A. Martellucci, and L. L. Shaw. Wall pressure fluctuations in attached boundary-layer flow. *AIAA Journal*, 21(4):495–502, 1983.

[2] J. E. Ffowcs-Williams. Surface pressure fluctuations induced by boundary layer flow at finite Mach number. *J. Fluid Mech.*, 22:507–519, 1965.

[3] P. Bradshaw. Inactive motion and pressure fluctuations in turbulent boundary layers. *J. Fluid Mech.*, 30(2):241–258, 1967.

[4] W. K. Blake. *Mechanics of Flow-Induced Sound and Vibration*. New York: Academic Press, 1986.

[5] T. M. Farabee and M. J. Casarella. Spectral features of wall pressure fluctuations beneath turbulent boundary layers. *Phys. Fluids A*, 3(10):2410–2420, 1991.

[6] S. P. Gravante, A. M. Naguip, C. E. Wark, and H. M. Nagib. Characterization of the pressure fluctuations under a fully developed turbulent boundary layer. *AIAA Journal*, 36(10):1808–1816, 1998.

[7] Y. Tsuji, J. H. N. Fransson, P. H. Alfredsson, and A. V. Johansson. Pressure statistics and their scaling in high-reynolds-number turbulent boundary layers. *J. Fluid Mech.*, 585:1–40, 2007.

[8] S. J. Beresh, J. F. Henfling, R. W. Spillers, and B. O. M. Pruett. Fluctuating wall pressures measured beneath a supersonic turbulent boundary layer. *Phys. Fluids*, 23(075110):1–16, 2011.

[9] M. Bernardini and S. Pirozzoli. Wall pressure fluctuations beneath supersonic turbulent boundary layers. *Phys. Fluids*, 23(085102):1–11, 2011.

[10] J. Poggie, N. J. Bisek, and R. Gosse. Resolution effects in compressible, turbulent boundary layer simulations. *Comput. Fluids*, 120:57–69, 2015.

[11] C. M. Helm and M. P. Martín. New LES of a Hypersonic Shock/Turbulent Boundary Layer Interaction. In *54th AIAA Aerospace Sciences Meeting*, pages 1–15, 2016.

[12] C. M. Helm and P. M. Martin. Görtler-like vortices in the LES Data of a mach 7 STBLI. In *55th AIAA Aerospace Sciences Meeting*, pages 1–13, 2017.

[13] V. Mikulla and C. C. Horstmann. Turbulence measurements in hypersonic shock-wave boundary layer interaction flows. *AIAA Journal*, 14(5):568–575, 1976.

[14] P. Bookey, C. Wyckham, A. J. Smits, and M. P. Martín. New experimental data of stbli at dns/les accesible Reynolds numbers. In *43rd AIAA Aerospace Sciences Meeting and Exhibit*, number AIAA 2005-309, pages 1–18, 2005.

[15] A. M. Schreyer, D. Sahoo, and A. J. Smits. Experimental investigations of a hypersonic shock turbulent boundary layer interaction. In *49th AIAA Aerospace Sciences Meeting*, number AIAA 2011-481, pages 1–12, 2011.

[16] A. M. Schreyer, D. Sahoo, and A. J. Smits. Turbulence measurements with PIV in a hypersonic shock boundary layer interaction. In *41st Fluid Dynamics Conference and Exhibit*, number AIAA 2011-3429, pages 1–14, 2011.

[17] L. Duan, I. Beekman, and M. P. Martín. Direct numerical simulation of hypersonic turbulent boundary layers. part 3. effect of mach number. *J. Fluid Mech.*, 672:245–267, 2011.

[18] K. J. Franko and S. K. Lele. Breakdown mechanisms and heat transfer overshoot in hypersonic zero pressure gradient boundary layers. *J. Fluid Mech.*, 730:491–532, 2013.

[19] L. Duan, M. M. Choudhari, and C. Zhang. Pressure fluctuations induced by a hypersonic turbulent boundary layer. *J. Fluid Mech.*, 804:578–607, 2016.

[20] K. Ritos, D. Drikakis, and I. W. Kokkinakis. Acoustic Loading beneath Hypersonic Transitional and Turbulent Boundary Layers. *J. Sound Vib.*, UNDER REVIEW, 2018.

[21] K. Ritos, I. W. Kokkinakis, and D. Drikakis. Physical insight into a mach 7.2 compression corner flow. In *AIAA Aerospace Sciences Meeting, Kissimmee, Florida*, 2018.

[22] D. Drikakis, M. Hahn, A. Mosedale, and B. Thornber. Large eddy simulation using high resolution and high order methods. *Proc. R. Soc. A*, 367:2985–2997, 2009.

[23] K. Ritos, I. W. Kokkinakis, D. Drikakis, and S. M. Spottswood. Implicit large eddy simulation of acoustic loading in supersonic turbulent boundary layers. *Phys. Fluids*, 29(4):1–11, 2017.

[24] K. Ritos, I. W. Kokkinakis, and D. Drikakis. Physical insight into the accuracy of iLES in turbulent boundary layers. *Comput. Fluids*, In Press, 2017.

[25] E. F. Toro, M. Spruce, and W. Speares. Restoration of the contact surface in the hll-riemann solver. *Shock Waves*, 4(1):25–34, 1994.

[26] E. F. Toro. *Riemann Solvers and Numerical Methods for Fluid Dynamics*. Springer, 3rd edition, 2009.
[27] D. S. Balsara and C. W. Shu. Monotonicity preserving weighted essentially non-oscillatory schemes with increasingly high order of accuracy. *J. Comput. Phys.*, 160(2):405–452, 2000.
[28] R. Spiteri and S. J. Ruuth. New class of optimal high-order strong-stability-preserving time discretization methods. *SIAM J. Numer. Anal.*, 40(2):469–491, 2002.
[29] V. Kolář. Compressibility effect in vortex identification. *AIAA Journal*, 47(2):473–475, 2009.
[30] V. Kolář and J. Šístek. Corotational and compressibility aspects leading to a modification of the vortex-identification q-criterion. *AIAA Journal*, 53(8):2406–2410, 2015.
[31] L. Duan and M. M. Choudhari. Numerical study of pressure fluctuations due to a mach 6 turbulent boundary layer. In *51st AIAA Aerospace Sciences Meeting*, pages 1–16, 2013.
[32] S. Stolz and N. A. Adams. Large-eddy simulation of high-reynolds-number supersonic boundary layers using the approximate deconvolution model and a rescaling and recycling technique. *Phys. Fluids*, 15(2398), 2003.
[33] S. Stolz. High-pass filtered eddy-viscosity models for large-eddy simulations of compressible wall-bounded flows. *J. Fluids Eng*, 127(4):666–673, 2005.
[34] I. Marusic, B. J. McKeon, P. A. Monkewitz, H. M. Nagib, A. J. Smits, and K. R. Sreenivasan. Wall-bounded turbulent flows at high reynolds numbers: Recent advances and key issue. *Phys. Fluids*, 22(065103), 2010.
[35] T. Gatski and J.-P. Bonnet. *Compressibility, Turbulence and High Speed Flow*. Academic Press, 2013.
[36] T. Maeder, N. A. Adams, and L. Kleiser. Direct simulation of turbulent supersonic boundary layers by an extended temporal approach. *J. Fluid Mech.*, 429:187–216, 2001.
[37] J. Blazek. *Fluid Dynamics, Principles and Applications*. Elsevier, 2015.
[38] T. S. Lund, X. Wu, and K. D. Squires. Generation of turbulent inflow data for spatially-developing boundary layer simulations. *J. Comput. Phys.*, 140:233–258, 1998.
[39] M. Klein, A. Sadiki, and J. Janicka. A digital filter based generation of inflow data for spatially developing direct numerical simulation or large eddy simulations. *J. Comput. Phys.*, 186:652–665, 2003.
[40] E. Touber and N. D. Sandham. Large-eddy simulation of low-frequency unsteadiness in a turbulent shock-induced separation bubble. *Theor. Comp. Fluid Dyn.*, 23:79–107, 2009.
[41] Z. A. Rana, B. Thornber, and D. Drikakis. Transverse jet injection into a supersonic turbulent cross-flow. *Phys. Fluids*, 23(046103):1–21, 2011.
[42] Z. A. Rana, B. Thornber, and D. Drikakis. On the importance of generating accurate turbulent boundary condition for unsteady simulations. *J. Turbul.*, 12(35):1–39, 2011.
[43] N. J. Georgiadis, D. P. Rizzetta, and C. Fureby. Large-eddy simulation: current capabilities, recommended practices, and future research. *AIAA Journal*, 48(8):1172–1784, 2010.
[44] H. Choi and P. Moin. Grid-point requirements for large eddy simulation: Chapman's estimates revisited. *Phys. Fluids*, 24:011702, 2012.
[45] R. D. Shattuck. Sound pressures and correlations of noise on the fuselage of a jet aircraft in flight. Technical Report TN-D-1086, NASA, 1961.
[46] W. W. Willmarth and C. E. Wooldridge. Measurements of the fluctuating pressure at the wall beneath a thick turbulent boundary layer. *J. Fluid Mech.*, 14(2):187–210, 1962.
[47] W. W. Willmarth and F. W. Roos. Resolution and structure of the wall pressure field beneath a turbulent boundary layer. *J. Fluid Mech.*, 22(1):81–94, 1965.
[48] M. K. Bull. Wall-pressure fluctuations associated with subsonic turbulent boundary layer flow. *J. Fluid Mech.*, 28(4):719–754, 1967.
[49] M. K. Bull. Wall-pressure fluctuations beneath turbulent boundary layers: Some reflections on forty years of research. *J. Sound Vib.*, 190(3):299–315, 1996.
[50] R. M. Lueptow. Transducer resolution and the turbulent wall pressure spectrum. *J. Acoust. Soc. Am.*, 97(1):370–378, 1995.
[51] M. C. Goody and R. L. Simpson. Surface pressure fluctuations beneath two= and three-dimensional turbulent boundary layers. *AIAA Journal*, 38(10):1822–1831, 2000.
[52] P. D. Welch. The use of Fast Fourier Transform for the estimation of power spectra: A method based on time averaging over short, modified periodograms. *IEEE Trans. Audio Electroacoust.*, AU-15:70–73, 1967.

[53] C. Zhang, L. Duan, and M. M. Choudhari. Effect of wall cooling on boundary-layer-induced pressure fluctuations at mach 6. *J. Fluid Mech.*, 822:5–30, 2017.
[54] R. H. Kraichnan. Pressure fluctuations in turbulent flow over a flat plate. *J. Acoust. Soc. Am.*, 28(3):378–390, 1956.
[55] O. M. Phillips. On the aerodynamic surface sound from a plane turbulent boundary. *Proc. R. Soc. A*, 234(1198):327–335, 1956.
[56] R. L. Panton and J. H. Linebarger. Wall pressure spectra calculations for equilibrium boundary layers. *J. Fluid Mech.*, 65(2):261–287, 1974.
[57] G. K. Batchelor. Pressure fluctuations in isotropic turbulence. *Proc. Camb. Phil. Soc.*, 47:359–374, 1951.
[58] G. Schewe. On the Structure and Resolution of Wall-Pressure Fluctuations Associated with Turbulent Boundary Layer Flow. *J. Fluid Mech.*, 134:311–328, 1983.
[59] Y. Tsuji and T. Ishihara. Similarity scaling of pressure fluctuation in turbulence. *Phys. Rev. E*, 68:026309, 2003.
[60] R. Camussi, M. felli, F. Pereira, G. Aloisio, and A. Di Marco. Statistical properties of wall pressure fluctuations over a forward-facing step. *Phys. Fluids*, 20:075113, 2008.
[61] J. Laufer. Some statistical properties of the pressure field radiated by a turbulent boundary layer. *Phys. Fluids*, 7(8):1191–1197, 1964.